Enhancement of Mn-N-C single atom catalysts via sulfur and/or oxygen co-doping for oxygen reduction in acidic conditions : unveiling the catalyst durability in fuel cells

Enhancement of Mn-N-C single atom catalysts via sulfur and/or oxygen co-doping for oxygen reduction in acidic conditions: Unveiling the catalyst durability in fuel cells

Parisa Nematollahi[*a], Erik C. Neyts[a]

[a] Research Group Plasmant, NANOlab Center of Excellence, Department of Chemistry, University of Antwerp, Universiteitsplein 1, 2610 Antwerp, Belgium

* Corresponding author. **Phone:** (+32) 32652346. **E-mail**: parisa.nematollahi@uantwerpen.be

Abstract

Carbon-supported single Mn sites coordinated with nitrogen (Mn-N-C) catalysts are amongst the most favorable platinum group metal-free (PGM-free) catalysts for proton exchange membrane fuel cells (PEMFCs). However, the high overpotential of these catalysts, limits their application for oxygen reduction reaction (ORR). Experiments showed that O and S heteroatom co-doping increases the catalytic activity of Mn-N-C catalysts for electrochemical gas conversion. This prompted us to perform a systematic investigation of the formed co-doped configurations at the atomic scale and to study the corresponding reaction mechanisms for oxygen reduction in acidic environment. All probable configurations for Mn-$N_xO_yS_z/C_{10}$ complexes are considered and the most stable and durable structures are selected as ORR active catalysts. Our results confirm the strong stabilization of the Mn sites over N_4- and N_3-doped carbonaceous support and consequently their stability against oxidation in contrast to other O and/or S co-doped heterostructures.

Keywords

Heteroatom doping, Oxygen reduction reaction, Mn-N-C catalyst, co-doping, fuel cell

Introduction

Great efforts have been done to develop novel, active, and efficient energy conversion and storage catalysts to meet the urgent need of the electronic industries for sustainable and renewable energy supply[1-2]. Proton-exchange membrane fuel cells (PMFCs) have been extensively studied for their low-cost and high energy densities [3-4]. One of the downsides of PEMFCs which hinders their development is the slow kinetics of the oxygen reduction reaction (ORR) [5-6]. Thus, developing novel, active, and efficient electrocatalysts is highly required. Besides carbon nanomaterials [7-9], single-atom catalysts (SACs), like metal-doped N_4 [10] and more specifically Fe-N-C catalysts, show promising activity for ORR in acidic environments [11-13] and they are highly desired to replace expensive platinum-based catalysts. However, they do not yet reach the requirements for the practical operation of PEMFCs [14-15]. The reason is that Fe ions increase the Fenton reactions, leading to the formation of large amounts of oxygen-containing radical species which significantly damage the triple-phase interface and the proton transfer pathways in PEMFCs [16] and consequently accelerate the PEMFC performance. Unlike Fe, Mn ions have a Fenton-inactivity character[17] and they rarely react with hydrogen peroxide. Therefore, Mn-N-C materials have been recently considered for catalyzing ORR[18-19] because MnN_4 active sites adsorb O_2 more actively while the O-O bond cleavage on these sites requires lower activation energy [20].

It is known that regulating the electronic structure and coordination environment of the metal sites with heteroatoms like O[21], S[22-23], or P[24] increases the electrocatalytic activity of the catalyst for ORR. This is known to be due to the larger atomic radius and high polarizability of S atoms relative to N atoms that can optimize the charge density and electron spin density of the doped material [25]. Another reason is that S-doping induces the charge distribution of the catalyst and consequently changes the chemisorption of oxygen, thus promoting the entire ORR process [26]. Furthermore, it is known that the lone pair of electrons on the 3p orbitals of the S atom causes a defect which makes the active site more suitable for accepting the O_2 lone pair during the ORR [27-29]. O- and N-atoms coordinated Mn-C_{10} cofactors have been synthesized and showed higher ORR activity comparable to Pt/C catalysts because O-doping can adjust the electronic structure of the original metal-N_4 catalyst to a more reasonable state [30]. Although the catalytic mechanisms of OER are studied for O-doping carbon materials [31], the accelerated activity for ORR is as yet disregarded

and its electronic effects on single metal-doped catalysts have not yet been investigated in detail [32-33].

Here, we use density functional theory (DFT) calculations to investigate all the possible distribution patterns of three different heteroatoms, i.e., N, O, and S coordinated with the single-Mn active site doped into a double-vacancy defective graphene surface. Then, the feasibility, activity, and selectivity of these catalysts are carefully investigated for ORR in acidic environments.

Computational details

All DFT calculations were performed using the Vienna Ab initio Simulation Package (VASP). The calculations are all spin-polarized, and based on the generalized gradient approximation of the Perdew-Burke-Ernzerhof functional, using a cut-off energy of 500 eV. Gaussian smearing with a smearing width of 0.01 eV is used in all geometry optimizations. The convergence criterion for the residual force and energy in structural relaxations was set to 0.01 eV/Å and 10^{-6} eV, respectively. Bader charge analysis is used to calculate the atomic charges and charge transfer [34]. The Γ-point-centered $6 \times 6 \times 1$ *k*-point mesh is used for sampling the Brillouin zone of the primitive unit cell. The DFT-D3 dispersion Grimme approximation is used [35] to include the weak dispersion interactions. The binding energy (ΔE_b) of the Mn-$N_xO_yS_z/C_{10}$ complexes is calculated as follows:

$$\Delta E_b = E_{Mn\text{-}NxOySz/C10} - E_{NxOySz/C10} - E_{Mn} \quad (1)$$

where $E_{Mn\text{-}NxOySz/C10}$, $E_{NxOySz/C10}$, and E_{Mn} are the total energy of the Mn-$N_xO_yS_z/C_{10}$ complex, defected $N_xO_yS_z/C_{10}$ complex, and the isolated single Mn atom, respectively. A more negative binding energy means a stronger binding of the Mn atom into the catalyst.

We calculate the free energy change of the adsorbed oxygenated species on each catalyst at zero potential and pH = 0 according to the proposed method of Nørskov [36] as $\Delta G = \Delta E + \Delta ZPE - T\Delta S + \Delta G_U$

where ΔE is the change in the total energy, ΔZPE is the change in the zero-point energy (ZPE), T is the temperature (298.15 K), and ΔS is the change in entropy. The ZPEs of the adsorbed ORR species were computed from DFT frequencies. For all adsorbed intermediates on the catalyst, only the vibrational entropy is taken into account because the translational and rotational degrees of

freedom of the adsorbate effectively convert into vibrational modes (frustrated translations and rotations). Notably, the sum of the translational, rotational, and vibrational contributions is considered for the gas phase molecules. ΔG_U is the free energy contribution related to the applied electrode potential (U) versus the reversible hydrogen electrode (RHE), i.e., $\Delta G_U = -neU$, where n is the number of H^+/e^- pairs transferred in ORR and e is the unit charge. The theoretical overpotential (η^{ORR}) is adopted as a measure of the whole ORR rate and is determined as $\eta^{ORR} = U_{equ} - (G^{ORR}/e)$, where G^{ORR} is the thermodynamic rate-determining step (RDS) for the ORR and the U_{equ} is the equilibrium potential of ORR reaction, $O_2(g) + 2H^+ + 2e^- \rightarrow 2H_2O$, which is taken from the tabulated experimental standard reduction potentials.

Results and discussion

Structural characterization of the catalysts

We start with the most well-known Mn-doped N_4-embedded graphene (MnN_4-C_{10}) structure. Then, the surrounding N atoms substitute with O, S, or a combination of two heteroatoms to make all possible configurations (see the 21 structures shown in Figure 1).

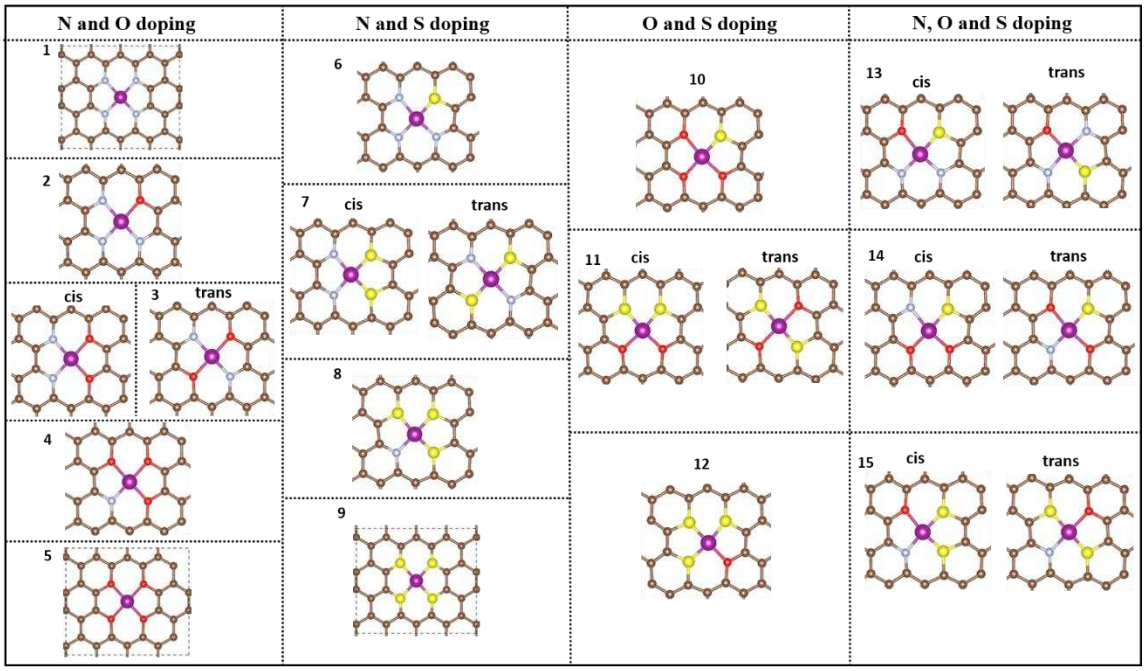

Figure 1. The optimized structures of doped MnN_4-C_{10} with S and O heteroatoms. The numbers refer to the rows mentioned in Table S1 showing the corresponding binding and formation energy of each structure. Color code: purple, Mn; blue, N; red, O; yellow, S, and brown, C.

The stability of each structure is determined by calculating the ΔE_b of the Mn atom into the structure and the formation energy (ΔE_f) of the complexes. The calculated values for more

energetically stable structures are listed in Table S1. A more negative ΔE_b, e.g., MnN_4-C_{10}, shows a stronger binding of the Mn atom into the structure of the catalyst, thus exhibiting promising stability of the configuration which is in close agreement with the synthesized structure [37]. The cohesive energy (ΔE_c) of the bulk Mn is calculated according to $\Delta E_c = \frac{1}{n} E_{\text{bulk Mn}} - E_{Mn}$, where n is the number of Mn atoms considered in the bulk Mn. The more negative ΔE_c shows a stronger binding of the Mn metal bulk. We calculate the formation energy (ΔE_f) of the doped complexes via $\Delta E_f = \Delta E_b - \Delta E_c$. A positive formation energy shows weaker binding of a single Mn atom into the defective substrate as compared to bulk Mn and therefore, it is more likely that Mn atoms agglomerate with other Mn atoms to form nanoparticles on the surface [38] (see Table S1). According to the obtained results, despite the negative value of the binding energy of the structures, their formation energy is positive except for MnN_4-C_{10} and MnN_3O-C_{10}. This shows that the Mn atom might agglomerate on the surface while catalyzing the redox reactions (see Figure 2). Therefore, after careful screening, the MnN_4-C_{10}, MnN_3O-C_{10}, and MnN_3S-C_{10} structures with ΔE_b of -6.75 eV, -5.03 eV, and -3.42 eV, respectively and ΔE_f values of -2.15 eV, -0.43 eV, and 1.18 eV, respectively, are selected for all further calculations. The binding energy and formation energy of the MnN_4-C_{10} catalyst is in good agreement with that of reported by Wang et al. [39] and Zhu et al. [40]. We further analyze the latter catalyst, MnN_3S-C_{10}, due to the high negative binding energy of Mn into the surrounding N_3O vacancy site. This will let us to compare its catalytic properties (with positive formation energy lower than that of other investigated catalysts in the list) with the results of MnN_4-C_{10} and MnN_3O-C_{10}.

We also investigated the electronic properties of the selected catalysts by calculating their total and partial density of states. The corresponding plots are shown in Figure S1 of the Supporting Information. One can see that by O and S doping a sharp peak appears at the Fermi level of MnN_3O-C_{10} and MnN_3S-C_{10}, respectively, which corresponds to the d and p orbitals of Mn and C atoms. According to the Bader charge analysis, the substitution of one N atom with one O or S increases the electron donation of the Mn atom. Compared to the MnN_4-C_{10}, in MnN_3O-C_{10}, the Mn charge decreases by about $|0.06|$ e while this decrease is more significant in MnN_3S-C_{10} by about $|0.26|$ e. The reason is that in MnN_3O-C_{10} both N and O atoms are electron acceptors while in MnN_3S-C_{10} both M and S atoms are donating electrons to the N atoms (see Table S2).

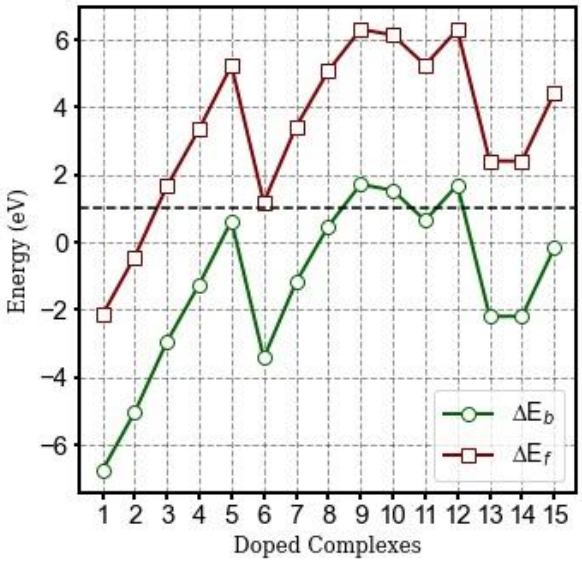

Figure 2. The calculated binding energy and formation energy of the doped complexes. The numbers on the x-axis refer to the row numbers in Table S1. The dashed line (y=1) is shown as a sign to show which configurations are selected as the more energetically stable structures.

Adsorption of oxygenated intermediates

We consider the ORR on acidic conditions based on Nafion electrolytes, by investigating the effects of SO_3^*/$^*SO_3H$ and the available $^*OH$ species, which is available in the system, as a ligand on ORR. Figures 3 and 4 show the binding energy of these ligands and ORR intermediates on the selected catalysts, respectively. One can see in Figure 3a that the $^*OH$ ligand has more negative binding energy on MnN_4-C_{10} and MnN_3O-C_{10} than those of SO_3^* and $^*SO_3H$, while SO_3^* adsorbs more strongly on MnN_3S-C_{10} than either *OH or $^*SO_3H$. According to the Sabatier principle [41-42], we expect that MnN_4-C_{10} shows better catalytic activity in the presence of $^*OH$ and $^*SO_3H$ due to their lower binding energy.

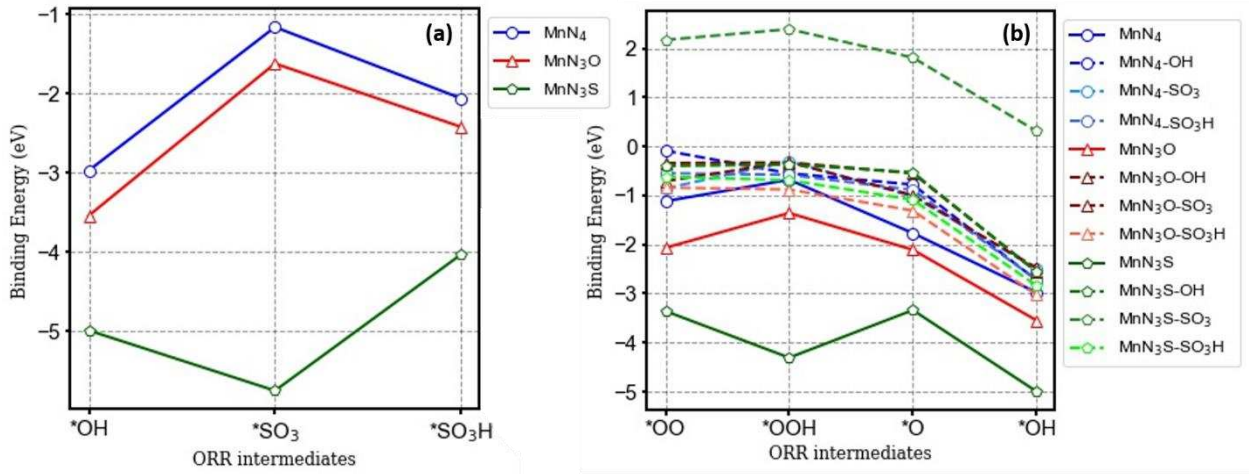

Figure 3. (a) Adsorption of ligands and (b) ORR intermediates on the selected catalysts.

To understand the performance of ORR in acidic conditions, we investigated the binding energy of all oxygenated intermediates (*OO, *OOH, *O, and *OH) on the complexes with and without the considered ligands (see Figure 3b). Our results indicate that all the oxygenated intermediates adsorb on pure (ligand-free) MnN_3S-C_{10} catalysts with higher (i.e., more negative) binding energy than that on MnN_4-C_{10} and MnN_3O-C_{10} with the order of MnN_3S-C_{10}>MnN_3O-C_{10}>MnN_4-C_{10}. One can see in Figures 3a and 3b that the adsorption difference of ligands and ORR species on ligand-free MnN_4-C_{10} and MnN_3O-C_{10} are in the range of $0.4<E_b<0.6$ and $0.3<E_b<0.9$ eV, respectively. Therefore, it can be concluded that both catalysts have similar electrocatalytic activity for ORR in an acidic environment.

In contrast to the pure catalysts, in the presence of the SO_3^-, SO_3H^-, and OH^- ligands, the binding energy of ORR intermediates reduces, and as shown in Figure 3b, the E_b difference of each ORR species on all the studied complexes is very small. The only exception is for MnN_3S-C_{10}@SO_3 where unlike the MnN_3S-C_{10}, MnN_3S-C_{10}@OH, and MnN_3S-C_{10}@SO_3H, the adsorption of ORR species on the Mn site is positive. According to Figures 3b and S3, the positive values suggest that ORR species are not strongly bound to the catalyst surface. Positive binding energies indicate that energy is required to adsorb these species onto the catalyst surface, rather than energy being released as typically observed in stable chemisorption. Therefore, the chemical bonds formed between the ORR species and the catalyst are relatively weak which makes the catalyst unstable during the ORR. Moreover, the presence of the SO_3 ligand on the Mn atom might interfere with the chemisorption of ORR species. In addition, one can see in Figure S3 that unlike MnN_3S-C_{10}@OH, and MnN_3S-C_{10}@SO_3H, in MnN_3S-C_{10}@SO_3 the Mn atom protrudes out of the surface, which might cause the degradation of the catalyst during the ORR process. In other catalysts, the ligand pulls down the Mn atom into the plane, reducing the Mn-N/Mn-S bond length and consequently making the catalyst more durable during the ORR. On the other hand, the SO_3 ligand is negatively charged due to its sulfonate group. If the ORR species carry a negative charge or have unfavorable charge distributions, the electrostatic repulsion between the negatively charged ligand and the ORR species can contribute to positive binding energies. This repulsion can make it energetically unfavorable for the ORR species to bind chemically to the catalyst.

In other catalysts, like MnN_3O-C_{10}@SO_3H, the SO_3H ligand contains a strongly acidic group (sulfonic acid), which can act as a proton donor. This can facilitate chemical interactions with the

ORR species, especially those that involve proton transfer steps. For example, in the case of OOH, which is a peroxo species ($OOH \rightarrow OOH + H^+ + e^-$), the SO_3H ligand might play a role in proton transfer, making chemical adsorption more favorable. In $MnN_3O\text{-}C_{10}$@OH catalyst, the OH ligand contains a hydroxyl group (OH), which can act as both a proton donor and acceptor. In ORR, proton transfer steps are essential for the conversion of oxygen molecules into water. The OH ligand can facilitate proton transfer reactions by donating or accepting protons during these processes, making it easier for ORR species like OOH, O, and OH to bind chemically which leads to negative binding energies.

We investigated and compared the Bader charge analysis for the selected catalysts with and without the ligands with an adsorbed OH* species on the Mn active center (see Table S2). In all of the configurations with different ligands, Mn donates electrons to both adsorbed *OH and the ligand. Moreover, in contrast to $MnN_3S\text{-}C_{10,}$ in $MnN_4\text{-}C_{10}$ and $MnN_3O\text{-}C_{10}$ the SO_3H ligand has the greatest charge accumulation. The total charge accumulation order on the ligands in $MnN_4\text{-}C_{10}$ and $MnN_3O\text{-}C_{10}$ catalysts is $SO_3H>SO_3>OH$ while is $SO_3H>OH>SO_3$ in $MnN_3S\text{-}C_{10}$. In $MnN_3S\text{-}C_{10}$ Mn atom has the highest charge depletion which can be due to the presence of the S atom as an electron donor (see Table S2). This might be the reason for the positive (weak) binding energy of ORR species on $MnN_3S\text{-}C_{10}$ shown in Figure 3b. However, the adsorbed *OH has the highest charge accumulation in the presence of OH ligand in all three catalysts.

Based on Sabatier's principle [41-42], a catalyst should have an affinity for the reactants, allowing them to adsorb onto the catalyst surface and undergo the desired chemical transformations. However, the catalyst should not bind the reactants too strongly, as this would hinder their release and the completion of the reaction. Therefore, we can conclude that $MnN_4\text{-}C_{10}$ can catalyze the ORR more actively than other catalysts in acidic conditions. The optimized structures of the adsorption species on $MnN_4\text{-}C_{10}$ along with the corresponding bond lengths are shown in Figure 4. The corresponding adsorption configurations on $MnN_3O\text{-}C_{10}$ and $MnN_3S\text{-}C_{10}$ are depicted in Figures S2 and S3 in the Supporting Information.

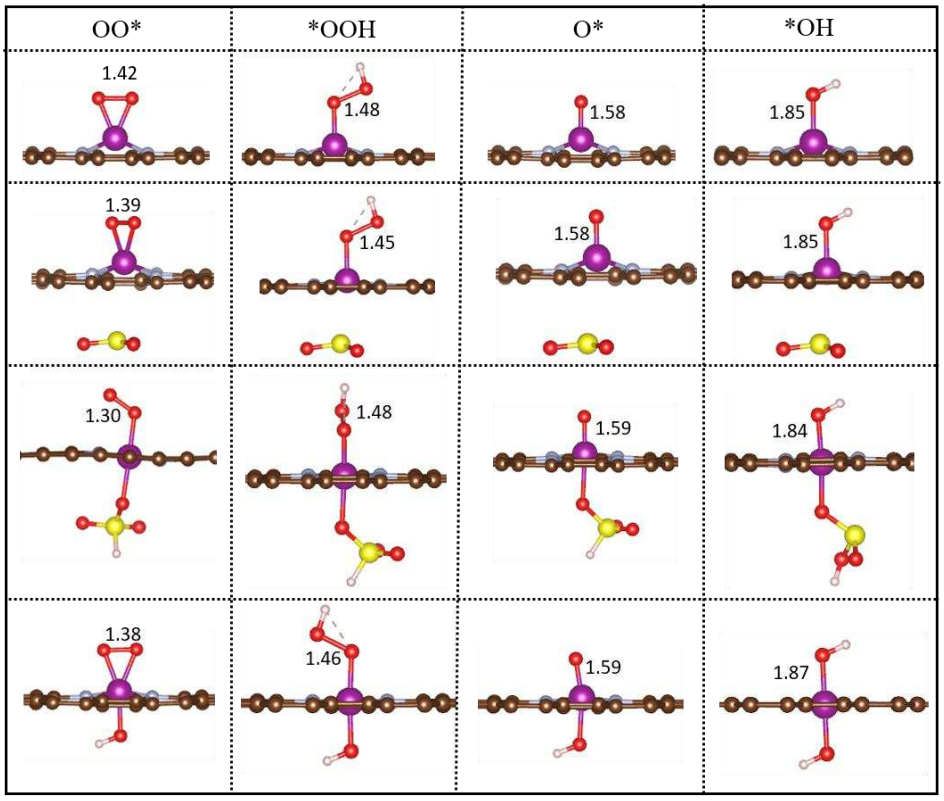

Figure 4. The optimized configurations of adsorbed ORR species on pure MnN_4-C_{10} catalyst, in the presence of $SO_3^-, SO_3H^-, and\ OH^-$ligands. All bond lengths are in angstrom Å. Color code: purple, Mn; blue, N; red, O; yellow, S, and brown, C.

Electrocatalytic ORR

To have a better understanding of the electrocatalytic activity of the selected catalysts for ORR and to compare the results with those of MnN_4-C_{10}, the ORR mechanism on MnN_3O-C_{10} and MnN_3S-C_{10} is also investigated in detail. The electrocatalytic ORR on MnN_4-C_{10}, MnN_3O-C_{10}, and MnN_3S-C_{10} at zero potential U = 0 V vs RHE, is validated by mechanistic investigations to construct the Gibbs free-energy diagrams, as displayed in Figures 5-7. The corresponding ORR configurations are presented in Figures 4, S2, and S3. In all diagrams, the black line is named "Ideal" as a representative of the ORR in equilibrium potential, 1.23 V vs RHE, proposed by Nørskov et al [36].

First, we start with the adsorption of O_2 on the active site of the surface. We considered two different orientations for the adsorbed O_2 species, *OO, on each catalyst i.e., end-on and side-on. Then, the more energetically favorable configuration is selected for starting the ORR. In all three catalysts, the side-on orientation of *OO is selected as the more stable adsorption configuration. Upon the adsorption of O_2 on pure catalysts, the O-O bond length increases by about 0.22 Å

compared to the O_2 gas molecule, 1.23 Å. This O-O bond elongation further increases in the first hydrogenation process where *OOH species form on the surfaces of MnN_4-C_{10} and MnN_3O-C_{10}. On MnN_3S-C_{10} the protonation step results in the O-O bond cleavage and formation of the *O and *OH both chemisorbed on the Mn active site. On the first two catalysts, the further hydrogenation steps lead to the formation of the *O and *OH moieties while the first and second H_2O molecules will be released from the surface in the third and fourth hydrogenation steps, respectively. The second protonation step of *O+*OH on MnN_3S-C_{10} may lead to the formation of *OH+*OH or *O + H_2O (see Figure S3). According to our investigation, the second path is the energetically more favorable pathway. The rest of the ORR is similar to the pathways on MnN_4-C_{10} and MnN_3O-C_{10} catalysts.

It can be seen in Figure 4 that in the pure structures, the Mn atom protrudes out of the surface causing a significant elongation of Mn-N, Mn-O, or Mn-S bond lengths. This bond elongation has a considerable effect on the stability of the catalysts during the ORR procedure. However, the Mn-N elongation in MnN_4-C_{10} is less than the elongations of the Mn-S and Mn-O bonds in MnN_3O-C_{10} and MnN_3S-C_{10}. Consequently, it can be expected that MnN_4-C_{10} can catalyze the ORR more actively than other catalysts. This is further confirmed by the calculated overpotential, which for pure MnN_4-C_{10}, MnN_3O-C_{10}, and MnN_3S-C_{10} structures is 1.02, 1.47, and 2.90 V vs RHE, respectively.

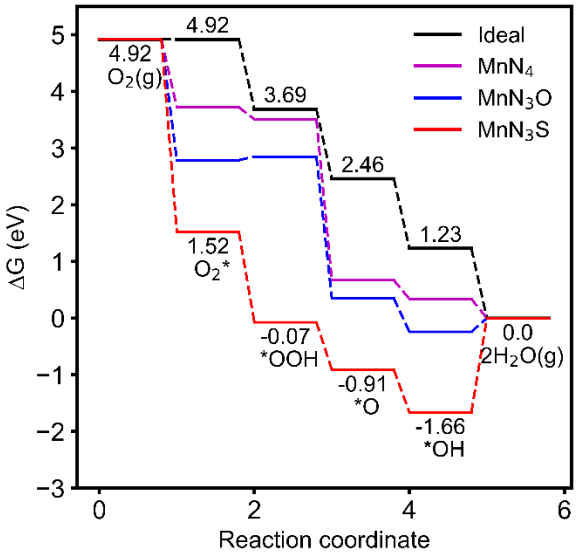

Figure 5. Gibbs free energy diagrams for ORR pathways on pure MnN_4-C_{10}, MnN_3O-C_{10}, and MnN_3S-C_{10}

The free energy diagram of the ORR on pure catalysts is shown in Figure 5. One can see that all the reduction reactions on MnN_4-C_{10} are exothermic while the formation of the second water molecule is endothermic on MnN_3O-C_{10} and MnN_3S-C_{10} and is, therefore, the RDS. In addition, as expected, MnN_3S-C_{10} has the lowest tendency to catalyze the ORR (red line) with the highest η^{ORR} while MnN_4-C_{10} energy states are closer to the ideal line (purple line) with the lowest η^{ORR}. It was discussed above and shown in Figures 3a and 3b that the binding energy of the ligands and ORR species on both MnN_4-C_{10} and MnN_3O-C_{10} has very small differences. This also complies with the corresponding free energy path of these two catalysts (see Figure 5). However, the obtained high values of the overpotentials and the Gibbs free energy states of pure catalysts deviating significantly from those of the ideal system, especially in MnN_3S-C_{10}, confirm that they are not ORR active. In the following, the details of the ORR in different conditions are explained in detail.

Considering $*SO_3$ and $SO_3{}^*H$ moieties (originating from Nafion electrolyte) as a fifth ligand, binding with Mn atom, improved the ORR activity of all the studied catalysts, by diminishing the Gibbs free energy states associated with each protonation step and approaching the energy states approximating the ideal linear trajectory, except for MnN_3S-C_{10}@SO_3 which is placed farther from the ideal line showing less tendency to catalyze ORR (see Figure 6a). According to the optimized configurations, shown in Figure 4, during the ORR procedure on MnN_4-C_{10}@SO_3 and MnN_4-C_{10}@SO_3H, the SO_3 ligand is physisorbed on the Mn site of the catalyst via its S atom while the SO_3H ligand binds chemically via its O atom to the Mn site. One can see that the side-on and end-on O_2 adsorption configuration is the more stable configuration in MnN_4-C_{10}@SO_3 and MnN_4-C_{10}@SO_3H, respectively. Upon the adsorption of O_2 on the active center of the catalyst, the O-O bond length increases from 1.20 to 1.39 (1.30) Å in MnN_4-C_{10}@SO_3 (MnN_4-C_{10}@SO_3H). The first protonation step leads to the formation of *OOH species where in both structures the O-O bond elongates to the average value of 1.47 Å. The first water molecule is released from the catalyst in the second protonation step where the atomic *O remains on the Mn site. The third protonation step converts the *O to *OH and the last step produces the second H_2O molecule, making the catalyst ready to start another ORR cycle in the system. In contrast to the pure MnN_4-C_{10} structure where the Mn atom protrudes out of the surface, in the presence of the SO_3 and SO_3H ligand, the Mn atom is pulled down by the ligand and stays in the plane which makes the catalyst more stable due to the considerable reduction of the Mn-N bond length (see Figure 4). The calculated η^{ORR} for

MnN_4-C_{10}@SO_3 and MnN_4-C_{10}@SO_3H is 1.20 and 0.60 V, respectively, which in comparison with that of pure MnN_4-C_{10} is decreased in the presence of SO_3H.

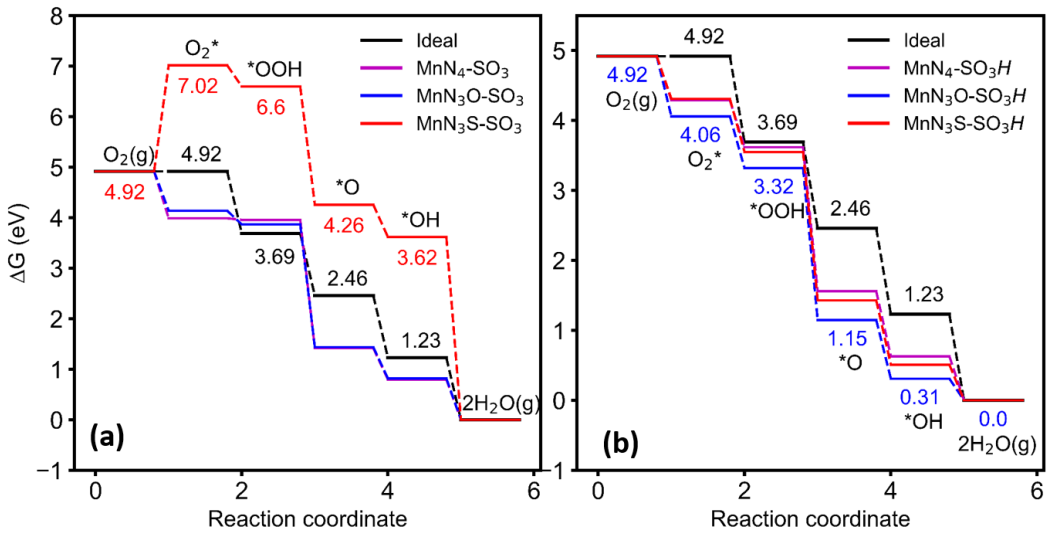

Figure 6. Gibbs free-energy diagrams for ORR pathways on MnN_4-C_{10}, MnN_3O-C_{10}, and MnN_3S-C_{10} structures at the presence of SO_3 (a) and SO_3H (b) ligands

O_2 adsorbs on MnN_3O-C_{10} and MnN_3S-C_{10} with the same orientation as on MnN_4-C_{10} in the presence of SO_3 and SO_3H ligands (see Figures S2 and S3). Like MnN_4-C_{10}, the SO_3 and SO_3H ligands physisorbed and chemisorbed on the Mn site of both MnN_3O-C_{10} and MnN_3S-C_{10} catalysts, respectively. The adsorption configurations of oxygen intermediates and $*O_2$ orientations on MnN_3O-C_{10} are similar to those of MnN_4-C_{10} while on MnN_3S-C_{10} except for the $*O_2$ orientations, both Mn and S atoms protrude out of the surface. More specifically, the Mn-S and C-S bond lengths are longer than the Mn-N bond lengths which is due to the larger atomic radius of the S atom. The same hydrogenation process as what occurs on MnN_4-C_{10}@SO_3 and MnN_4-C_{10}@SO_3H happens on MnN_3O-C_{10}@SO_3 and MnN_3O-C_{10}@SO_3H while on MnN_3S-C_{10}@SO_3, the O-O bond length increases significantly, to 1.42 Å, upon adsorption on the Mn site. This causes the complete cleavage of the O-O bond in the first hydrogenation step forming the atomic oxygen and hydroxyl radical, $*OO + (H^+ + e^-) \rightarrow *O + 0H^{\cdot}$. Therefore, the next hydrogenation step might be the formation of $*O+H_2O$ or $*OH+0H^{\cdot}$. Our results show that the energetically more favorable pathway is the first path, shown in Figure S3. One can see in Figure 6a that in the presence of SO_3 ligand, unlike the MnN_3S-C_{10}, the ORR process is more active on MnN_4-C_{10} and MnN_3O-C_{10} with similar Gibbs free energy states all close to those of the ideal line. Interestingly, all three catalysts showed good electrocatalytic activity for ORR in the presence of SO_3H ligand (see Figure 6b). This can be

confirmed by the calculated η^{ORR} for MnN_3O-C_{10}@SO_3, MnN_3O-C_{10}@SO_3H, MnN_3S-C_{10}@SO_3, and MnN_3S-C_{10}@SO_3H that is 0.96, 0.92, 0.80, and 0.72 V vs RHE, respectively.

Unlike SO_3 and SO_3H species, the adsorption of *OH as a fifth ligand on the active Mn sites has a higher effect on the electrocatalytic ORR of the studied catalysts (see Figure 7). The side-on adsorption configuration is the dominant configuration of *OO on all three catalysts. The *OOH, *O, and *OH species form on the catalysts during the protonation steps where all the reactions are exothermic and energetically favorable at ambient conditions, except for the O_2 adsorption on MnN_4-C_{10} which is slightly endothermic. The desorption of H_2O and the first hydrogenation step of *OO is the RDS on MnN_4-C_{10}@OH and MnN_3O-C_{10}@OH / MnN_3S-C_{10}@OH. One can see in Figure 7 that in the presence of *OH, all three catalysts are ORR active. As we expected, the MnN_4-C_{10}@OH and MnN_3O-C_{10}@OH have closer energy states to those of the ideal line.

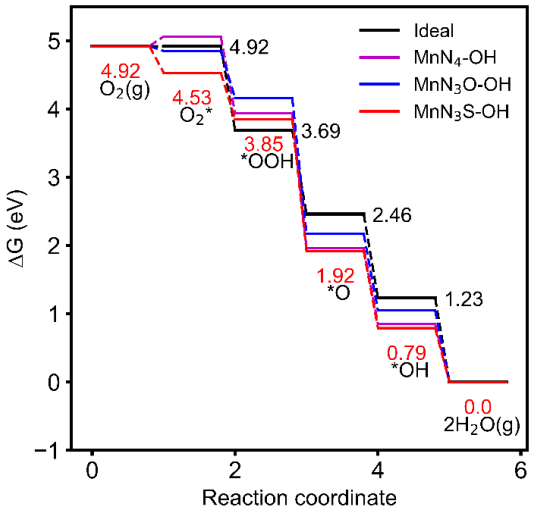

Figure 7. Gibbs free-energy diagrams for ORR pathways on MnN_4-C_{10}@OH, MnN_3O-C_{10}@OH, and MnN_3S-C_{10}@OH

The calculated η^{ORR} for MnN_4-C_{10}@OH, MnN_3O-C_{10}@OH, and MnN_3S-C_{10}@OH catalysts is significantly reduced to 0.38, 0.53, and 0.55 V, respectively (see Figure 8). Therefore, we confirm that the ORR is more actively proceeding when the *OH species is adsorbed on the Mn center and acts as a fifth ligand. This makes the structures more stable, durable, and catalytically active for ORR and significantly reduces the theoretical ORR overpotential of the catalysts specifically for MnN_4-C_{10} and MnN_3O-C_{10} (see Figure 8).

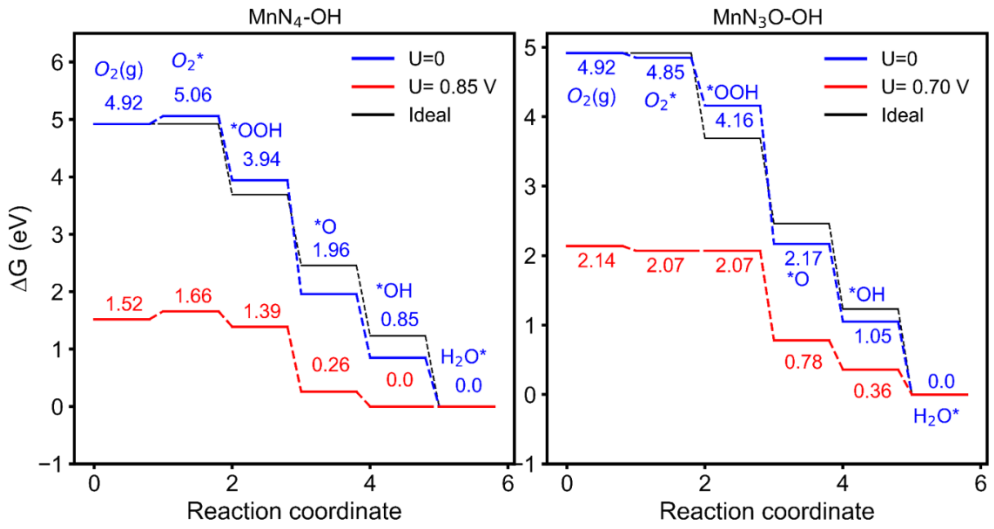

Figure 8. Gibbs free-energy diagrams for ORR pathways on MnN_4-C_{10}@OH and MnN_3O-C_{10}@OH catalysts at U=0 and the applied potential

Conclusion

Although experiments demonstrated that doping O or S in Mn-N-C catalysts increases the CO_2 reduction reaction activity[43], and ORR [44-45], a systematic theoretical investigation studying the details of the doping and reduction reaction in an acidic environment was missing. Here, we performed DFT calculations to investigate the ORR activity of a series of MnN_4-C_{10} structures doped with O and S heteroatoms in an acidic environment. Two major steps were analyzed carefully: (i) screening the series of optimized modified structures to find the most stable configuration that can catalyze the ORR, and (ii) finding the ORR mechanism on each catalyst with and without the ligand ($SO_3^-, SO_3H^-,$ and OH^-). We conclude that doping O and/or S heteroatoms into the MnN_4-C_{10} structure reduces the stability and catalytic activity of the catalysts for ORR except for the selected three structures i.e., MnN_4-C_{10} and MnN_3O-C_{10} and MnN_3S-C_{10}. In contrast to the MnN_3S-C_{10}, the role of the fifth ligand is to pull back the Mn atom into the basal plane during the ORR preventing the elongation of the Mn-N bond. This reduces the possibility of the catalyst's degradation during the reduction process. More specifically, the MnN_4-C_{10} and MnN_3O-C_{10} catalyst exhibits both durability and ORR activity in the presence of the *OH species as a fifth ligand with a significant overpotential value of 0.38 and 0.53 V, respectively. Our study provides guidance for rational SAC designs and opportunities for efficient ORR strategies.

Acknowledgments

P.N. and E.C.N. gratefully acknowledge the support by the Fund of Scientific Research Flanders (FWO), Belgium, Grant number 1261721N. The computational resources and services used in this work were provided by the HPC core facility CalcUA of the Universiteit Antwerpen and VSC (Flemish Supercomputer Center), funded by the FWO and the Flemish Government.

References

1. Li, X.; Guan, B. Y.; Gao, S.; Lou, X. W. D., A general dual-templating approach to biomass-derived hierarchically porous heteroatom-doped carbon materials for enhanced electrocatalytic oxygen reduction. *Energy Environ. Sci.* **2019,** *12* (2), 648-655.

2. Yang, J.; Ju, Z.; Jiang, Y.; Xing, Z.; Xi, B.; Feng, J.; Xiong, S., Enhanced capacity and rate capability of nitrogen/oxygen dual-doped hard carbon in capacitive potassium-ion storage. *Adv. Mater.* **2018,** *30* (4), 1700104.

3. Ji, H.; Wang, M.; Liu, S.; Sun, H.; Liu, J.; Qian, T.; Yan, C., In-situ observation as activity descriptor enables rational design of oxygen reduction catalyst for zinc-air battery. *Energy Storage Materials* **2020,** *27*, 226-231.

4. Qu, X.; Han, Y.; Chen, Y.; Lin, J.; Li, G.; Yang, J.; Jiang, Y.; Sun, S., Stepwise pyrolysis treatment as an efficient strategy to enhance the stability performance of Fe-NX/C electrocatalyst towards oxygen reduction reaction and proton exchange membrane fuel cell. *Appl. Catal. B-Environ.* **2021,** *295*, 120311.

5. Yu, J.; Zhou, Q.; Xue, X.; Zhang, H.; Li, X.; Wang, F.; Chen, Q.; Zhu, H., Development of a highly stable Pt-based ORR catalyst over Mn-modified polyaniline-based carbon nanofibers. *New J. Chem.* **2021,** *45* (32), 14608-14615.

6. Nie, Y.; Li, L.; Wei, Z., Achievements in Pt nanoalloy oxygen reduction reaction catalysts: Strain engineering, stability and atom utilization efficiency. *ChemComm* **2021,** *57* (96), 12898-12913.

7. Fan, F.; Hui, Y.; Devasenathipathy, R.; Peng, X.; Huang, Q.; Xu, W.; Yang, F.; Liu, X.; Wang, L.; Chen, D.-H., Composition-adjustable Mo6Co6C2/Co@ carbon nanocage for enhanced oxygen reduction and evolution reactions. *Journal of Colloid and Interface Science* **2023,** *636*, 450-458.

8. Fan, F.; Huang, Q.; Devasenathipathy, R.; Peng, X.; Yang, F.; Liu, X.; Wang, L.; Chen, D.-H.; Fan, Y.; Chen, W., Composite-structure-defined nitrogen-doped carbon nanocage embedded Co/CoxP for enhanced oxygen reduction and evolution reactions. *Electrochim. Acta* **2023,** *437*, 141514.

9. Huang, K.; Zhang, W.; Li, J.; Fan, Y.; Yang, B.; Rong, C.; Qi, J.; Chen, W.; Yang, J., In situ anchoring of zeolite imidazole framework-derived Co, N-doped porous carbon on multiwalled carbon nanotubes toward efficient electrocatalytic oxygen reduction. *ACS Sustainable Chemistry & Engineering* **2019,** *8* (1), 478-485.

10. Jiang, Z.; Liu, X.; Liu, X.-Z.; Huang, S.; Liu, Y.; Yao, Z.-C.; Zhang, Y.; Zhang, Q.-H.; Gu, L.; Zheng, L.-R., Interfacial assembly of binary atomic metal-Nx sites for high-performance energy devices. *Nat. Commun.* **2023,** *14* (1), 1822.

11. Kramm, U. I.; Herranz, J.; Larouche, N.; Arruda, T. M.; Lefevre, M.; Jaouen, F.; Bogdanoff, P.; Fiechter, S.; Abs-Wurmbach, I.; Mukerjee, S.; Dodelet, J. P., Structure of the catalytic sites in Fe/N/C-catalysts for O2-reduction in PEM fuel cells. *Phys. Chem. Chem. Phys.* **2012,** *14* (33), 11673-88.

12. Jia, Q.; Ramaswamy, N.; Hafiz, H.; Tylus, U.; Strickland, K.; Wu, G.; Barbiellini, B.; Bansil, A.; Holby, E. F.; Zelenay, P., Experimental observation of redox-induced Fe–N switching behavior as a determinant role for oxygen reduction activity. *ACS Nano* **2015,** *9* (12), 12496-12505.

13. Zhong, J.-P.; Hou, C.; Sun, M.-L.; Yang, Z.-Y.; Chen, D.-H.; Fan, Y.-J.; Chen, W.; Liao, H.-G.; Sun, S.-G., A superior electrocatalyst toward the oxygen reduction reaction obtained by atomically dispersing copper on N, F co-doped graphene through atomic interface engineering. *J. Mater. Chem. A* **2022,** *10* (26), 13876-13883.

14. Du, L.; Prabhakaran, V.; Xie, X.; Park, S.; Wang, Y.; Shao, Y., Low-PGM and PGM-free catalysts for proton exchange membrane fuel cells: stability challenges and material solutions. *Adv. Mater.* **2021,** *33* (6), 1908232.

15. Zhang, H.; Chung, H. T.; Cullen, D. A.; Wagner, S.; Kramm, U. I.; More, K. L.; Zelenay, P.; Wu, G., High-performance fuel cell cathodes exclusively containing atomically dispersed iron active sites. *Energy Environ. Sci.* **2019,** *12* (8), 2548-2558.

16. Li, Y.; Wang, H.; Priest, C.; Li, S.; Xu, P.; Wu, G., Electrocatalysis: Advanced Electrocatalysis for Energy and Environmental Sustainability via Water and Nitrogen Reactions (Adv. Mater. 6/2021). *Adv. Mater.* **2021,** *33* (6), 2170042.

17. Zhong, Y.; Liang, X.; He, Z.; Tan, W.; Zhu, J.; Yuan, P.; Zhu, R.; He, H., The constraints of transition metal substitutions (Ti, Cr, Mn, Co and Ni) in magnetite on its catalytic activity in heterogeneous Fenton and UV/Fenton reaction: From the perspective of hydroxyl radical generation. *Appl. Catal. B-Environ.* **2014,** *150*, 612-618.

18. Li, G.-L.; Lu, Z.-F.; Wang, X.; Cao, S.; Hao, C., Rational Construction of Atomically Dispersed Mn-N x Embedded in Mesoporous N-Doped Amorphous Carbon for Efficient Oxygen Reduction Reaction in Zn-Air Batteries. *ACS Sustainable Chemistry & Engineering* **2021,** *10* (1), 224-233.

19. Xu, H.; Wang, D.; Yang, P.; Liu, A.; Li, R.; Li, Y.; Xiao, L.; Zhang, J.; An, M., A theoretical study of atomically dispersed MN 4/C (M= Fe or Mn) as a high-activity catalyst for the oxygen reduction reaction. *Phys. Chem. Chem. Phys.* **2020,** *22* (48), 28297-28303.

20. Liu, K.; Qiao, Z.; Hwang, S.; Liu, Z.; Zhang, H.; Su, D.; Xu, H.; Wu, G.; Wang, G., Mn- and N-doped carbon as promising catalysts for oxygen reduction reaction: Theoretical prediction and experimental validation. *Appl. Catal. B-Environ.* **2019,** *243*, 195-203.

21. Duan, X.; Pan, N.; Sun, C.; Zhang, K.; Zhu, X.; Zhang, M.; Song, L.; Zheng, H., MOF-derived Co-MOF, O-doped carbon as trifunctional electrocatalysts to enable highly efficient Zn–air batteries and water-splitting. *Journal of Energy Chemistry* **2021,** *56*, 290-298.

22. Xu, H.; Wang, D.; Yang, P.; Liu, A.; Li, R.; Xiao, L.; Zhang, J.; Qu, Z.; An, M., FeS encapsulated hierarchical porous S, N-dual-doped carbon for oxygen reduction reaction facilitation in Zn–air batteries. *Sustainable Energy & Fuels* **2021,** *5* (10), 2695-2703.

23. Yao, P.; Cao, J.; Gong, X.; Han, C.; Ruan, M.; Song, P.; Xu, W., ZIF-Derived Co–N–S Tridoped Carbon Frameworks for Electrocatalytic Oxygen Reduction Reaction. *J. Phys. Chem. C.* **2021,** *125* (18), 9839-9846.

24. Li, J.-C.; Zhong, H.; Xu, M.; Li, T.; Wang, L.; Shi, Q.; Feng, S.; Lyu, Z.; Liu, D.; Du, D., Boosting the activity of Fe-Nx moieties in Fe-NC electrocatalysts via phosphorus doping for oxygen reduction reaction. *Science China Materials* **2019,** *63* (6).

25. Asefa, T., Metal-free and noble metal-free heteroatom-doped nanostructured carbons as prospective sustainable electrocatalysts. *Acc. Chem. Res.* **2016,** *49* (9), 1873-1883.

26. Fu, C.; Luo, L.; Yang, L.; Shen, S.; Wei, G.; Zhang, J., Breaking the scaling relationship of ORR on carbon-based single-atom catalysts through building a local collaborative structure. *Catal. Sci. Technol* **2021,** *11* (23), 7764-7772.

27. Huang, X.; Shen, T.; Sun, S.; Hou, Y., Synergistic modulation of carbon-based, precious-metal-free electrocatalysts for oxygen reduction reaction. *ACS Appl. Mater. Interfaces* **2021,** *13* (6), 6989-7003.

28. Wang, Y. C.; Lai, Y. J.; Song, L.; Zhou, Z. Y.; Liu, J. G.; Wang, Q.; Yang, X. D.; Chen, C.; Shi, W.; Zheng, Y. P., S-doping of an Fe/N/C ORR catalyst for polymer electrolyte membrane fuel cells with high power density. *Angew. Chemi.* **2015,** *127* (34), 10045-10048.

29. Zhang, J.; Zhao, Y.; Chen, C.; Huang, Y.-C.; Dong, C.-L.; Chen, C.-J.; Liu, R.-S.; Wang, C.; Yan, K.; Li, Y., Tuning the coordination environment in single-atom catalysts to achieve highly efficient oxygen reduction reactions. *Journal of the American Chemical Society* **2019,** *141* (51), 20118-20126.

30. Yang, Y.; Mao, K.; Gao, S.; Huang, H.; Xia, G.; Lin, Z.; Jiang, P.; Wang, C.; Wang, H.; Chen, Q., O-, N-atoms-coordinated Mn cofactors within a graphene framework as bioinspired oxygen reduction reaction electrocatalysts. *Adv. Mater.* **2018,** *30* (28), 1801732.

31. Li, L.; Yang, H.; Miao, J.; Zhang, L.; Wang, H.-Y.; Zeng, Z.; Huang, W.; Dong, X.; Liu, B., Unraveling oxygen evolution reaction on carbon-based electrocatalysts: effect of oxygen doping on adsorption of oxygenated intermediates. *ACS Energy Letters* **2017,** *2* (2), 294-300.

32. Silva, R.; Voiry, D.; Chhowalla, M.; Asefa, T., Efficient metal-free electrocatalysts for oxygen reduction: polyaniline-derived N-and O-doped mesoporous carbons. *Journal of the American Chemical Society* **2013,** *135* (21), 7823-7826.

33. Meng, Y.; Voiry, D.; Goswami, A.; Zou, X.; Huang, X.; Chhowalla, M.; Liu, Z.; Asefa, T., N-, O-, and S-tridoped nanoporous carbons as selective catalysts for oxygen reduction and alcohol oxidation reactions. *Journal of the American Chemical Society* **2014,** *136* (39), 13554-13557.

34. Bader, R., Atoms in Molecules: A Quantum Theory 1990. *There is no corresponding record for this reference.[Google Scholar]* **1998**.

35. Grimme, S.; Antony, J.; Ehrlich, S.; Krieg, H., A consistent and accurate ab initio parametrization of density functional dispersion correction (DFT-D) for the 94 elements H-Pu. *J. Chem. Phys.* **2010,** *132* (15), 154104.

36. Nørskov, J. K.; Rossmeisl, J.; Logadottir, A.; Lindqvist, L.; Kitchin, J. R.; Bligaard, T.; Jonsson, H., Origin of the overpotential for oxygen reduction at a fuel-cell cathode. *J. Phys. Chem. B.* **2004,** *108* (46), 17886-17892.

37. Liu, S.; Wang, M.; Yang, X.; Shi, Q.; Qiao, Z.; Lucero, M.; Ma, Q.; More, K. L.; Cullen, D. A.; Feng, Z., Chemical vapor deposition for atomically dispersed and nitrogen coordinated single metal site catalysts. *Angew. Chem.* **2020,** *59* (48), 21698-21705.

38. Qian, Y.; Liu, Y.; Zhao, Y.; Zhang, X.; Yu, G., Single vs double atom catalyst for N2 activation in nitrogen reduction reaction: a DFT perspective. *EcoMat* **2020,** *2* (1), e12014.

39. Wang, Y.; Shao, M., Theoretical screening of transition metal–N4-doped graphene for electroreduction of nitrate. *ACS Catal.* **2022,** *12* (9), 5407-5415.

40. Zhu, G.; Liu, F.; Wang, Y.; Wei, Z.; Wang, W., Systematic exploration of N, C coordination effects on the ORR performance of Mn–N x doped graphene catalysts based on DFT calculations. *Phys. Chem. Chem. Phys.* **2019,** *21* (24), 12826-12836.

41. Sabatier, P., *La catalyse en chimie organique*. 1920.

42. Sabatier, P., La Catalyse En Chimie Organique; Encyclopédie de science chimique appliquée. *Ch Béranger* **1913**.

43. Kossmann, J.; Sánchez-Manjavacas, M. L. O.; Brandt, J.; Heil, T.; López-Salas, N.; Albero, J., Mn (ii) sub-nanometric site stabilization in noble, N-doped carbonaceous materials for electrochemical CO 2 reduction. *ChemComm* **2022,** *58* (31), 4841-4844.

44. Guo, L.; Hwang, S.; Li, B.; Yang, F.; Wang, M.; Chen, M.; Yang, X.; Karakalos, S. G.; Cullen, D. A.; Feng, Z., Promoting atomically dispersed MnN4 sites via sulfur doping for oxygen reduction: unveiling intrinsic activity and degradation in fuel cells. *ACS Nano* **2021,** *15* (4), 6886-6899.

45. Bhange, S. N.; Unni, S. M.; Kurungot, S., Graphene with Fe and S coordinated active centers: an active competitor for the Fe–N–C active Center for Oxygen Reduction Reaction in acidic and basic pH conditions. *ACS Applied Energy Materials* **2018,** *1* (2), 368-376.

Enhancement of Mn-N-C single atom catalysts via sulfur and/or oxygen co-doping for oxygen reduction in acidic conditions: Unveiling the catalyst durability in fuel cells

Parisa Nematollahi[*a], Erik C. Neyts[a]

[a] Research Group Plasmant, NANOlab Center of Excellence, Department of Chemistry, University of Antwerp, Universiteitsplein 1, 2610 Antwerp, Belgium

* Corresponding author. **Phone:** (+32) 32652346. **E-mail**: parisa.nematollahi@uantwerpen.be

Table S1. The calculated changes of the binding energy (ΔE_b) and formation energy (ΔE_f) of different possible Mn doped $N_xO_yS_z$ configurations.

Row	Complex	ΔE_b (eV)	ΔE_f (eV)	Row	Complex	ΔE_b (eV)	ΔE_f (eV)
1	MnN_4-G	-6.75	-2.15	9	MnS_4-G	1.72	6.31
2	MnN_3O-G	-5.03	-0.43	10	MnO_3S	1.54	6.14
3	MnN_2O_2-G (trans)	-2.94	1.66	11	MnS_2O_2 (cis)	0.65	5.25
4	$MnNO_3$-G	-1.24	3.36	12	$MnOS_3$	1.70	6.30
5	MnO_4-G	0.64	5.24	13	MnN_2OS (N cis)	-2.19	2.41
6	MnN_3S-G	-3.42	1.18	14	$MnNO_2S$ (O-cis)	-2.19	2.41
7	MnN_2S_2-G (cis)	-1.18	3.42	15	$MnNOS_2$ (S-cis)	-0.17	4.42
8	$MnNS_3$-G	0.48	5.08				

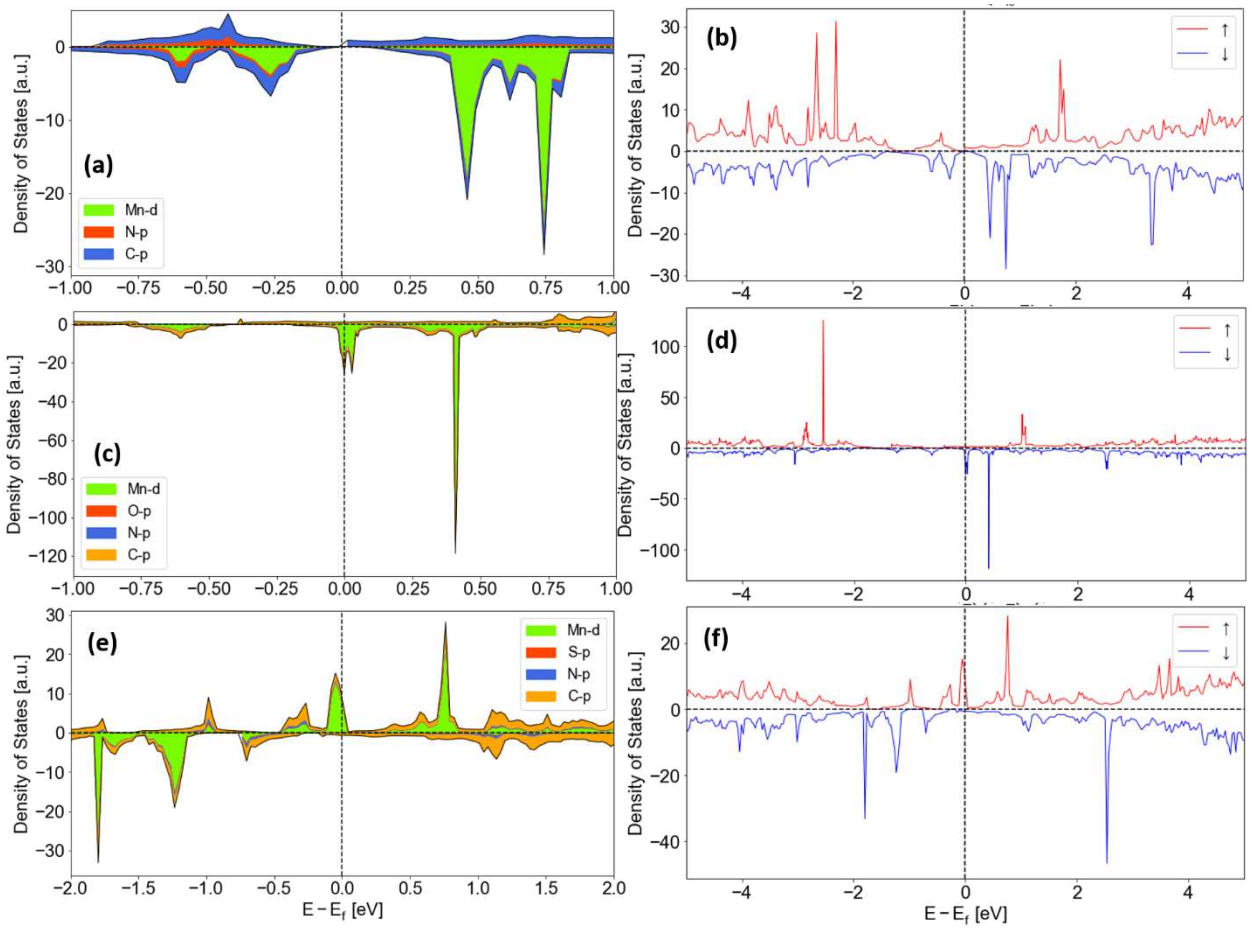

Figure S1. The PDOS (a, c, e) and TDOS (b, d, f) plot of optimized MnN_4-C_{10} (a,b), MnN_3O-C_{10} (c,d), and MnN_3S-C_{10} (e,f).

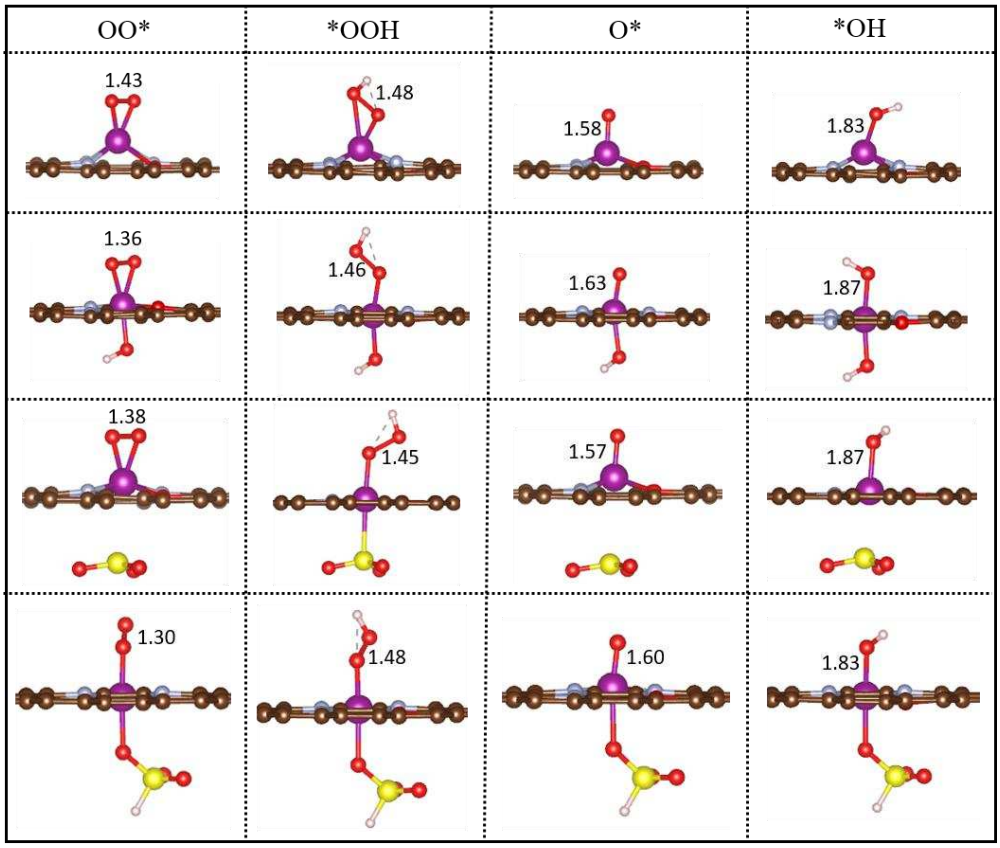

Figure S2. The optimized configurations of adsorbed ORR species on pure MnN_3O-C_{10} catalyst, at the presence of $SO_3^-, SO_3H^-, and\ OH^-$ligands. All bond lengths are in angstrom Å. Color code: purple, Mn; blue, N; red, O; yellow, S, and brown, C.

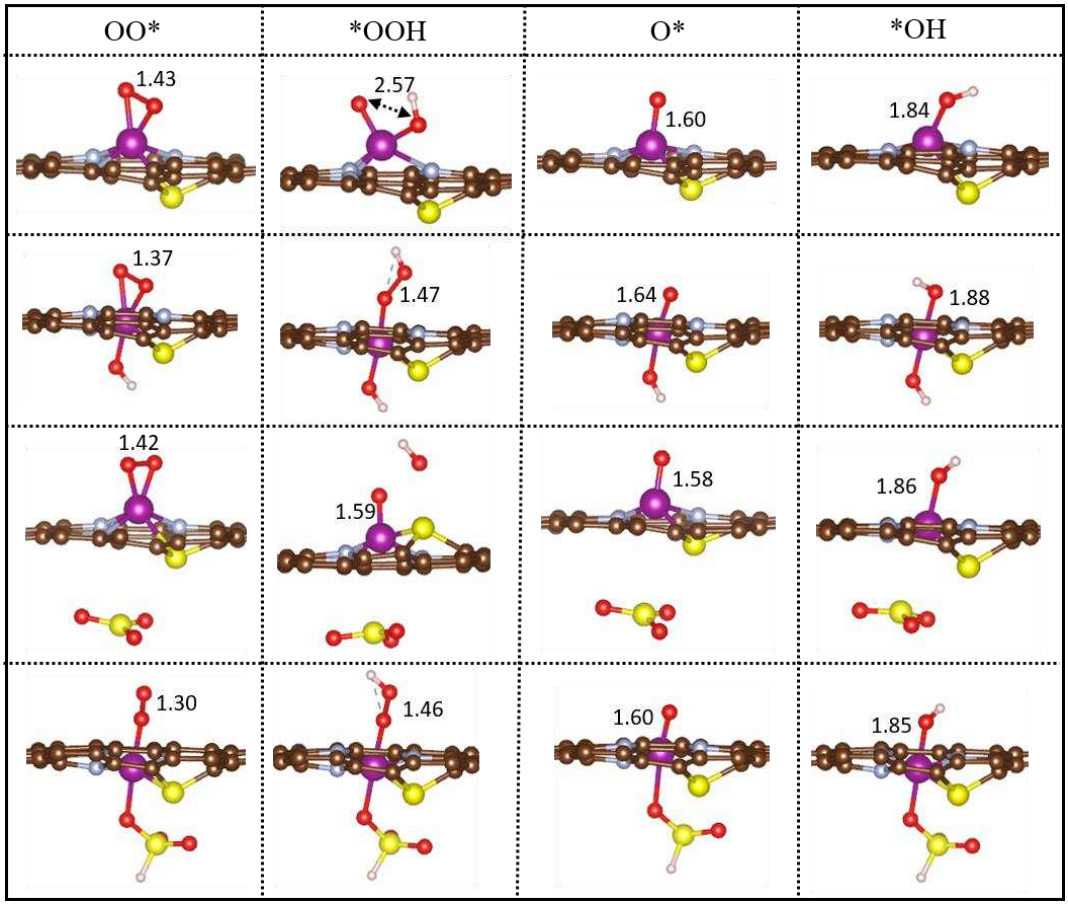

Figure S3. The optimized configurations of adsorbed ORR species on pure MnN_3S-C_{10} catalyst, at the presence of $SO_3^-, SO_3H^-, and\ OH^-$ligands. All bond lengths are in angstrom Å. Color code: purple, Mn; blue, N; red, O; yellow, S, and brown, C.

Table S2. The calculated Bader charge analysis (q)

Complex	Bader charges (q)							
	Mn	N_{surf}	O_{surf}	S_{surf}	OH	OH_{lig}	$SO_{3(lig)}$	SO_3H_{lig}
MnN_4-C_{10}	1.29	-1.20	-	-	-	-	-	-
MnN_3O-C_{10}	1.23	-1.18	-1.08	-	-	-	-	-
MnN_3S-C_{10}	1.03	-1.18	-	0.32	-	-	-	-
MnN_4OH-C_{10}	1.44	-1.16	-	-	-0.48	-	-	-
MnN_3OOH-C_{10}	1.46	-1.20	-1.10	-	-0.54	-	-	-
MnN_3SOH-C_{10}	1.41	-1.20	-		-0.52	-	-	-
MnN_4OH-C_{10}@OH	1.61	-1.11	-	-	-0.58	-0.43	-	-
MnN_3OOH-C_{10}@OH	1.53	-1.20	-1.10	-	-0.52	-0.53	-	-
MnN_3SOH-C_{10}@OH	1.43	-1.10	-	0.15	-0.53	-0.51	-	-
MnN_4OH-C_{10}@SO_3	1.42	-1.18	-	-	-0.45	-	-0.51	-
MnN_3OOH-C_{10}@ SO_3	1.42	-1.13	-1.05	-	-0.48	-	-0.68	-
MnN_3SOH-C_{10}@ SO_3	1.31	-1.22	-	0.13	-0.52	-	-0.34	-
MnN_4OH-C_{10}@SO_3H	1.56	-1.20	-	-	-0.46	-	-	-0.63
MnN_3OOH-C_{10}@ SO_3H	1.49	-1.10	-1.08	-	-0.46	-	-	-0.74
MnN_3SOH-C_{10}@ SO_3H	1.37	-1.11	-	0.23	-0.43	-	-	-0.73